Journal of Science and Transport Technology
Journal homepage: https://jstt.vn/index.php/en

Experimental LQR Control for a Double-Linked Inverted Pendulum on Cart

Truong-Phuong-Nam Pham[1], Trong-Bang Tran[2], Duc-Anh-Quan Nguyen[3], Vi-Do Tran[1], Van-Thuyen Ngo[1], Tran-Minh-Nguyet Nguyen[1], Van-Dong-Hai Nguyen[1,*], Trung-Thang Nguyen[1,4], Hari Maghfiroh[5], Minh-Tam Nguyen[1]

[1]Ho Chi Minh City University of Technology and Engineering (HCM-UTE), No.01 Vo Van Ngan Street, Thu Duc ward, Ho Chi Minh City 700000, Vietnam

[2]Department of Mechanical Engineering, Konkuk University, Seoul 05029, Republic of Korea

[3]Ho Chi Minh City University of Technology (HCMUT), Vietnam National University Ho Chi Minh City (VNU-HCM), 258 Ly Thuong Kiet Street, District 10, Ho Chi Minh City 700000, Vietnam

[4]Cao Thang Technical College, 65 Huynh Thuc Khang Street, Ben Nghe Ward, District 1, Ho Chi Minh City 700000, Vietnam

[5]Universitas Sebelas Maret (UNS), Ir. Sutami Street 36A Kentingan, Jebres, Surakarta, Central Java 57126, Indonesia

Article info
Type of article:
Original research paper

DOI:
https://doi.org/10.58845/jstt.utt.2026.en.6.2.354-374

***Corresponding author:**
Email address:
hainvd@hcmute.edu.vn

Received: 24/09/2025
Received in Revised Form: 31/03/2026
Accepted: 29/05/2026

Abstract: This paper presents an experimental study on the stabilization of a double inverted pendulum on a cart using a Linear Quadratic Regulator controller. Building upon previous simulation-based research, the current work focuses on the practical implementation of the LQR control strategy on a real laboratory setup. The mathematical model of the system was first derived using Lagrangian dynamics and validated through simulations to ensure accuracy. An LQR controller was then designed and implemented on an experimental platform consisting of a DC motor, encoder sensors, and a real-time control unit. The experimental results clearly demonstrate the capability of the LQR controller to stabilize both pendulum links in the upright position while maintaining bounded cart motion and acceptable energy consumption. Furthermore, a systematic comparison between simulation and experimental results is provided, showing strong agreement and confirming the robustness of the proposed approach. This study highlights the feasibility of applying LQR control in real-world underactuated systems and provides a solid foundation for future research on advanced and intelligent control strategies, including nonlinear and adaptive methods.

Keywords: Double inverted pendulum, SIMO system, LQR control, underactuated system, experimental validation, stabilization.

1. Introduction

The double-linked inverted pendulum on cart (DIPC) is an extension of the classical single inverted pendulum system [1], [2]. It consists of two interconnected pendulum links mounted on a moving cart (cart–pole IPC). This system is highly nonlinear, unstable, underactuated, and multivariable, and it may even exhibit chaotic behavior. Without an appropriate control strategy, the system can easily fall from its equilibrium

position [3]. Due to these challenging characteristics, the DIPC has been widely used as a benchmark platform for evaluating various advanced control methods. In addition, the mechanical structure of the DIPC is similar to many practical engineering systems such as robotic manipulators, walking robots, and aerospace mechanisms. Therefore, studying this system is not only important from a theoretical perspective but also highly relevant to real-world applications [4].

The DIPC can be considered a nonlinear single-input multi-output (SIMO) system that requires an appropriate multivariable control strategy to maintain balance [5]. Furthermore, C.–H. Nguyen et al. (2024) reported that adding a second pendulum link significantly increases the system order and complexity, making the double inverted pendulum a representative challenge in modern control engineering [6]. To stabilize such a dynamic system, various control approaches have been proposed, including optimal control, robust control, and intelligent control methods [7]–[12].

Among these approaches, the Linear Quadratic Regulator (LQR) has been widely used due to its optimal control formulation and systematic design procedure [13-15]. The LQR controller determines an optimal feedback gain matrix by minimizing a quadratic cost function, which allows the system states to converge to the equilibrium point while balancing control performance and control effort. In addition, LQR offers several practical advantages for real-world implementation, such as structural simplicity, computational efficiency, and guaranteed closed-loop stability around the linearized equilibrium point. These characteristics make LQR particularly suitable for real-time control of underactuated systems implemented on embedded hardware platforms.

In addition to classical optimal control methods, intelligent control techniques such as the Adaptive Neuro-Fuzzy Inference System (ANFIS) have also been investigated for inverted pendulum systems because of their ability to approximate nonlinear relationships and learn from data [16-19]. Numerous studies have proposed different control strategies for inverted pendulum systems in both single and double configurations [20]–[24]. However, many of these studies mainly focus on simulation results, while experimental validation on real hardware platforms remains relatively limited [25, 26]. Experimental implementation is particularly challenging for double inverted pendulum systems due to sensor noise, actuator limitations, and modeling uncertainties.

A few studies have attempted experimental validation of control strategies. For example, the work in [27] implemented an LQR-based controller on a double inverted pendulum system. However, the reported stabilization duration was relatively short, and the system could maintain balance for less than 3 seconds. This limitation indicates that achieving stable and sustained balancing performance in real experimental conditions remains a challenging task. Therefore, further experimental investigations are required to verify the practical feasibility and robustness of control algorithms for complex systems such as the DIPC.

In our previous work [28, 29], a mathematical model of the DIPC system was developed based on forward kinematics theory [30], and both LQR and ANFIS controllers were investigated through simulation studies. The simulation results demonstrated that these controllers were capable of stabilizing the system and provided promising control performance. However, that study mainly focused on numerical validation, and the feasibility of implementing the controllers on a real experimental platform was not addressed.

Motivated by these limitations, this paper focuses on the experimental implementation and validation of the LQR controller on a real DIPC platform. The dynamic equations and the basic simulation framework developed in [29] are briefly revisited to provide the theoretical foundation for

the present study. This study presents an experimental investigation of stabilizing a DIPC using a LQR. Unlike previous works that mainly focus on simulation, this paper emphasizes real-world implementation and validation on a physical hardware platform. The main contributions include: (i) experimental implementation of an LQR controller on an embedded STM32-based DIPC system; (ii) an improved controller tuning strategy that enhances cart stabilization while reducing control effort; and (iii) a quantitative evaluation through simulation–experiment comparison using RMSE metrics. The experimental results confirm reliable stabilization under real operating conditions.

Therefore, the main objective of this work is to bridge the gap between simulation and real-world implementation by experimentally validating the LQR controller for the DIPC system. The experimental responses are analyzed and compared with the simulation results in order to evaluate the controller's practical performance and to identify the differences between theoretical predictions and real-system behavior. Since the LQR controller represents a fundamental linear optimal control strategy, its successful experimental implementation provides an essential baseline for developing and validating more advanced intelligent control approaches in future research.

The remainder of this paper is organized as follows. Section 2 presents the mathematical model of the DIPC system. Section 3 describes the design of the LQR controller and simulation results. Section 4 presents the experimental setup and experimental results. Finally, Section 5 concludes the paper.

2. Mathematical equations and simulation

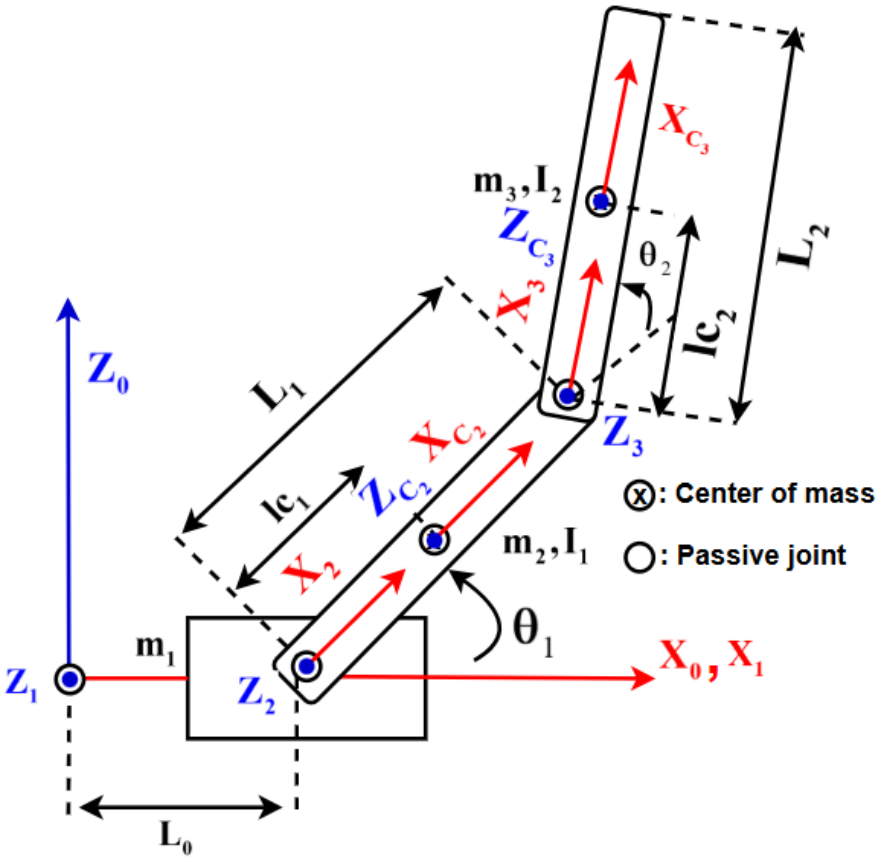

Fig. 1. Structure of the system [29]

2.1. The mathematical equations

First, it is necessary to establish the mathematical model in order to analyze the system and derive the motion of the entire setup. In the actual system, a GT2 belt drive mechanism is employed. The motor receives a voltage signal to

generate torque and is connected to a pulley with a 3:1 transmission ratio, meaning that three motor revolutions correspond to one pulley revolution. Two identical pulleys are installed at both ends to drive the cart back and forth. The system is visualized in Fig. 1, where a reference coordinate system is defined. This coordinate system serves as the frame of reference for the DIPC, enabling the application of kinematic methods based on robot theory [30]. The derived kinematic equations are then used as the foundation for further analysis and modeling of the system dynamics. The coordinate system is defined as shown in Fig. 1, where we introduce additional coordinate frames c_2 and c_3 to determine the center of mass of the pendulums. The coordinate frame assignment method is based on the Modified-DH convention presented in [30]. The DIPC can be regarded as a three-degree-of-freedom underactuated robotic system. Therefore, adopting this well-established method was considered appropriate in our study.

The parameters in Table 1 summarizes the physical parameters of the experimental DIPC setup. The cart mass and pendulum link masses were measured directly, while the inertia values were calculated using rigid-body dynamics. The distances from the pivot to the center of mass of each link were obtained experimentally, ensuring that the model accurately reflects the real hardware. These parameters provide the essential foundation for deriving the kinematic equations. Together with the coordinate frame assignment illustrated in Fig. 1, the system can be analyzed using robot kinematics theory, thereby enabling a consistent formulation of the subsequent dynamic model.

Table 1. Parameters of system

Parameters	Description	Values
θ_1	Link 1 deviation angle	radian
θ_2	Link 2 deviation angle	radian
L_0	Translational displacement of the cart	m
m_1	The mass of cart	0.491 Kg
m_2	The mass of link 1	0.172 Kg
m_3	The mass of link 2	0.055 Kg
I_0	The moment of inertia of cart	0 $Kg.m^2$
I_1	The moment of inertia of link 1	0.0033 $Kg.m^2$
I_2	The moment of inertia of link 2	0.0017 $Kg.m^2$
L_1	Length of link 1	0.1875 m
L_2	Length of link 2	0.278 m
l_{c1}	Link 1 center of mass distance from the pivot	0.1265 m
l_{c2}	Link 2 center of mass distance from the pivot	0.154 m
d	Pulley pitch diameter radius	0.0191044 m
g	Acceleration of gravity	9.81 m/s^2
f_1	Applied force on the cart	N

In our previous study [29], we developed the kinematic model of the system based on the forward kinematics theory introduced by J. Craig [30]. This approach offers the advantage of establishing a strong correlation between the state variables in the computation of kinetic and potential energies. Moreover, it proves to be effective and scalable when applied to systems with a higher number of degrees of freedom.

From the Euler–Lagrange equations previously formulated [29], the general form of the state equation can be obtained:

$$M(q)\ddot{q} + C(q,\dot{q})\dot{q} + G(q) = F \quad (1)$$

where:

$$M(q) = M(l_0, \theta_1, \theta_2) = \begin{bmatrix} \frac{\partial \tau_1}{\partial \ddot{l}_0} & \frac{\partial \tau_1}{\partial \ddot{\theta}_1} & \frac{\partial \tau_1}{\partial \ddot{\theta}_2} \\ \frac{\partial \tau_2}{\partial \ddot{l}_0} & \frac{\partial \tau_2}{\partial \ddot{\theta}_1} & \frac{\partial \tau_2}{\partial \ddot{\theta}_2} \\ \frac{\partial \tau_2}{\partial \ddot{l}_0} & \frac{\partial \tau_3}{\partial \ddot{\theta}_1} & \frac{\partial \tau_3}{\partial \ddot{\theta}_2} \end{bmatrix} \in R^{3\times 3}$$: is inertia matrix

$$F = \begin{bmatrix} \tau_1 \\ \tau_2 \\ \tau_3 \end{bmatrix} = \begin{bmatrix} \frac{d}{dt}\left(\frac{\partial L}{\partial \dot{l}_0}\right) - \frac{\partial L}{\partial l_0} \\ \frac{d}{dt}\left(\frac{\partial L}{\partial \dot{\theta}_1}\right) - \frac{\partial L}{\partial \theta_1} \\ \frac{d}{dt}\left(\frac{\partial L}{\partial \dot{\theta}_2}\right) - \frac{\partial L}{\partial \theta_2} \end{bmatrix} \in R^{3\times 1}$$: is force vector

$\tau_1(t)$: Applied force on cart

$\tau_2(t)$: Torque acting on the first pendulum

$\tau_3(t)$: Torque acting on the second pendulum

$$\ddot{q} = \begin{bmatrix} \ddot{L}_0 \\ \ddot{\theta}_1 \\ \ddot{\theta}_2 \end{bmatrix} \in R^{3\times 1}; \dot{q} = \begin{bmatrix} \dot{L}_0 \\ \dot{\theta}_1 \\ \dot{\theta}_2 \end{bmatrix} \in R^{3\times 1}; q = \begin{bmatrix} L_0 \\ \theta_1 \\ \theta_2 \end{bmatrix} \in R^{3\times 1}$$ is state variables vector of DIPC system

For simplicity, the frictional disturbance is neglected, and the system is considered to be influenced solely by the input τ_1.

The acceleration equation is rewritten from the state equation as follows:

$$\ddot{q} = M(q)^{-1}\left(F - \left(C(q,\dot{q})\dot{q} + G(q)\right)\right) \quad (2)$$

where:

$$C(q,\dot{q})\dot{q} + G(q) = \left(F - M(q)\ddot{q} = \begin{bmatrix} \tau_1 \\ \tau_2 \\ \tau_3 \end{bmatrix} - M(q)\ddot{q}\right) \in R^{3\times 1}$$

denote the Coriolis matrix and the gravity vector

By substituting these components into Eq. (2), we get:

$$\begin{bmatrix} \ddot{L}_0 \\ \ddot{\theta}_1 \\ \ddot{\theta}_2 \end{bmatrix} = \begin{bmatrix} \frac{\partial \tau_1}{\partial \ddot{L}_0} & \frac{\partial \tau_1}{\partial \ddot{\theta}_1} & \frac{\partial \tau_1}{\partial \ddot{\theta}_2} \\ \frac{\partial \tau_2}{\partial \ddot{L}_0} & \frac{\partial \tau_2}{\partial \ddot{\theta}_1} & \frac{\partial \tau_2}{\partial \ddot{\theta}_2} \\ \frac{\partial \tau_3}{\partial \ddot{L}_0} & \frac{\partial \tau_3}{\partial \ddot{\theta}_1} & \frac{\partial \tau_3}{\partial \ddot{\theta}_2} \end{bmatrix}^{-1}$$

$$\left[\begin{bmatrix} \tau_1 \\ \tau_2 \\ \tau_3 \end{bmatrix} - \left(\begin{bmatrix} \frac{d}{dt}\left(\frac{\partial L}{\partial \dot{L}_0}\right) - \frac{\partial L}{\partial L_0} \\ \frac{d}{dt}\left(\frac{\partial L}{\partial \dot{\theta}_1}\right) - \frac{\partial L}{\partial \theta_1} \\ \frac{d}{dt}\left(\frac{\partial L}{\partial \dot{\theta}_2}\right) - \frac{\partial L}{\partial \theta_2} \end{bmatrix} - \begin{bmatrix} \frac{\partial \tau_1}{\partial \ddot{L}_0} & \frac{\partial \tau_1}{\partial \ddot{\theta}_1} & \frac{\partial \tau_1}{\partial \ddot{\theta}_2} \\ \frac{\partial \tau_2}{\partial \ddot{L}_0} & \frac{\partial \tau_2}{\partial \ddot{\theta}_1} & \frac{\partial \tau_2}{\partial \ddot{\theta}_2} \\ \frac{\partial \tau_3}{\partial \ddot{L}_0} & \frac{\partial \tau_3}{\partial \ddot{\theta}_1} & \frac{\partial \tau_3}{\partial \ddot{\theta}_2} \end{bmatrix} \begin{bmatrix} \ddot{L}_0 \\ \ddot{\theta}_1 \\ \ddot{\theta}_2 \end{bmatrix}\right)\right] \quad (3)$$

Subsequently, MATLAB was employed to support the computational process. Since MATLAB does not provide direct differentiation with respect to time, the Jacobian formulation presented in document [30] was applied to construct a sequence of partial derivatives for the composite function, as shown in the following equation:

$$\dot{Y} = J(\beta)\dot{N} \quad (4)$$

where:

$\dot{Y}$: The time derivative of the output vector

$J(\beta)$: The Jacobian matrix of output with respect to the input vector

$\dot{N}$: The time derivative of the input vector

Since the linearization process has been described in detail in [29], only the discrete-time linearized matrices are briefly presented here.

Linearizing the system, we obtain matrix A, B:

$$\begin{bmatrix} \dot{L}_0 \\ \dot{\theta}_1 \\ \dot{\theta}_2 \end{bmatrix} = A \begin{bmatrix} L_0 \\ \theta_1 \\ \theta_2 \end{bmatrix} + B \begin{bmatrix} \tau_1 \\ \tau_2 \\ \tau_3 \end{bmatrix} \quad (5)$$

The system is discretized using a sampling period of 5 milliseconds.

$$[Ad, Bd] = c2d(A, B, 0.005) \quad (6)$$

$$Ad = \begin{bmatrix} 1 & 0.005 & 0 & 0 & 0 & 0 \\ 0 & 1 & 0.0146 & 0 & 0.0012 & 0 \\ 0 & 1 & 1.0006 & 0.005 & -0.0001 & 0 \\ 0 & 0 & 0.2274 & 1.0006 & -0.0328 & -0.0001 \\ 0 & 0 & -0.0004 & 0 & 1.0004 & 0.005 \\ 0 & 0 & -0.1729 & -0.0004 & 0.1787 & 1.0004 \end{bmatrix} \quad (7)$$

$$Bd = \begin{bmatrix} 0 & 0.009 & 0.0001 & 0.0323 & -0.0001 & -0.0245 \end{bmatrix}^T \quad (8)$$

Before designing the controller, it is necessary to verify the controllability of the system by determining the rank of the matrix in Eq. (9). If the rank of the matrix matches the number of state variables, the model is considered controllable. The matrix is presented as follows:

$$T = \begin{bmatrix} Bd & AdBd & Ad^2Bd & Ad^3Bd & Ad^4Bd & Ad^5Bd \end{bmatrix} \quad (9)$$

$$T = \begin{bmatrix} 0 & 0.0001 & 0.0001 & 0.0002 & 0.0002 & 0.0002 \\ 0.0090 & 0.0090 & 0.0090 & 0.0091 & 0.0091 & 0.0091 \\ 0.0001 & 0.0002 & 0.0004 & 0.0006 & 0.0007 & 0.0009 \\ 0.0323 & 0.0323 & 0.0324 & 0.0325 & 0.0327 & 0.0329 \\ -0.0001 & -0.0002 & -0.0003 & -0.0004 & -0.0006 & -0.0007 \\ -0.0245 & -0.0246 & -0.0247 & -0.0248 & -0.0250 & -0.0253 \end{bmatrix} \quad (10)$$

By determining the rank of the matrix in Eq. (10), we obtain:

$$Rank(T) = 6 \quad (11)$$

The result in Eq. (11) confirms that the system is controllable.

2.2. LQR controller

The DIPC system is described by the linear state-space equation as follows:

$$\dot{x}(t) = Ax(t) + Bu(t) \quad (12)$$

where:

$$x(t): \begin{bmatrix} x_1(t) & x_2(t) & x_3(t) & x_4(t) & x_5(t) & x_6(t) \end{bmatrix}^T \in R^{6\times 1}$$

$$\left(x_1 = l_0, x_2 = \dot{l}_0, x_3 = \theta_1, x_4 = \dot{\theta}_1, x_5 = \theta_2, x_6 = \dot{\theta}_2\right)$$

$$u(t): \begin{bmatrix} \tau_1(t) & \tau_2(t) & \tau_3(t) \end{bmatrix}^T \in R^{3\times 1}$$

Objective is to determine the input vector 'u', so as to minimize the performance index:

$$J(u) = \frac{1}{2}\int_0^\infty \left(x^T(t)Qx(t) + u^T(t)Ru(t)\right)dt \quad (13)$$

Let $Q \geq 0$ and $R \succ 0$. The control input $u(t)$ is selected to minimize the quadratic performance index in Eq. (13). Under these conditions, the state-feedback law:

$$u = -K * x \quad (14)$$

is optimal for any initial state x_0. Here, P is the solution of the continuous-time algebraic Riccati equation, and the optimal gain is given by $K = -R^{-1}B^TP$. Consequently, the remaining task is to solve the Riccati equation [21].

$$A^TP + PA - PBR^{-1}B^TP + Q = 0 \quad (15)$$

In our previous work [29], we obtained the state feedback gain matrix K. Since the cart position response was not entirely satisfactory, a Genetic Algorithm (GA) was later employed to optimize these parameters, where Q and R are determined Q=diag[(0.896396 15.6706 0.651927 0.1181 0.792001 0.9599)], R=[0.796955] yielding an improved feedback gain matrix K as follows:

$$K = R^{-1}B^TP = \begin{bmatrix} K_{L_0} & K_{\dot{L}_0} & K_{\theta_1} & K_{\dot{\theta}_1} & K_{\theta_2} & K_{\dot{\theta}_2} \end{bmatrix} \quad (16)$$

The gain matrix K is computed using the discrete-time LQR method via MATLAB's function:

$$K = dlqr(Ad, Bd, Q, R) \quad (17)$$

The computed state feedback gain matrix K is:

K_{L_0} = 0.9763; $K_{\dot{L}_0}$ = 4.9193; K_{θ_1} = -30.8268;

$K_{\dot{\theta}_1}$ = -15.2867; K_{θ_2} = -136.3463; $K_{\dot{\theta}_2}$ = -24.7514.

Fig. 2 illustrates the block diagram of the LQR controller used in this study. In the diagram, x is the state vector, u is the control input, and y is the output vector. The feedback gain matrix K is designed to minimize a quadratic performance index as defined in Eq. (13). This structure follows the standard LQR formulation in document [21].

Although both the state feedback controller and the Linear Quadratic Regulator (LQR) share the same control law $u = -K * x$, their design methodologies differ significantly. In conventional state feedback, the gain matrix K is chosen mainly through pole placement, which ensures stability but often relies on heuristic tuning and does not guarantee optimal performance. In contrast, the LQR systematically determines K by solving an optimization problem that minimizes a quadratic cost function in Eq. (13), thereby achieving an explicit trade-off between state regulation accuracy and control effort. This optimality makes LQR more robust and effective for practical applications compared to simple state feedback.

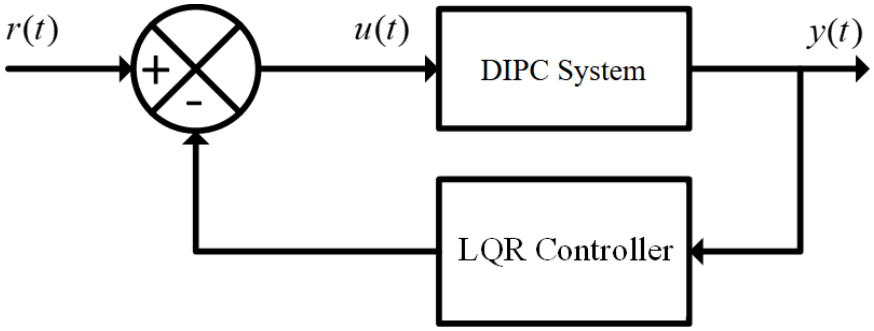

Fig. 2. LQR controller structure [28]

2.3. Simulation program

System overview:

The structure of the system in the simulation environment is depicted through block diagrams, as shown in Fig. 3.

Most system simulations are carried out under ideal conditions. To narrow the gap between simulation and practical implementation, an encoder block is placed at the angular output to reduce the resolution of the signal delivered to the controller. By differentiating the encoder output, the velocity signal obtained corresponds to what a real microcontroller would measure. In practice, however, this differentiation process reduces the effective resolution of the measured signal, which also depends on the quality of the encoder. In contrast, traditional simulations compute velocity by integrating the acceleration, thereby producing a velocity signal with a resolution that is effectively higher than that of the angular position data. This discrepancy is one of the reasons why controllers that perform well in simulations often fail to deliver similar results in experiments, aside from the fundamental requirement of accurate system parameter identification.

Cart's encoder:

The encoder block simulates a physical encoder with a resolution of 1000 pulses (step = 1000). The cart position output is fed into the encoder block and converted into pulses to simplify the computation and round the values into integers. Subsequently, this data is converted back into meters and provided at the output, as illustrated in Fig. 4 and the conversion between meters and pulses is expressed in by the following equation:

$$\text{pulse} = \frac{\alpha * \text{step} * 4}{d * \pi} \quad (18)$$

where:

α : The measured cart position signal (m)

step : Encoder resolution (pulses per round)

d : The pulley pitch diameter (m)

Encoder of the first and second pendulum:

Similarly, two additional encoder blocks are implemented to simulate the real encoder signals, each with a resolution of 1000 pulses per revolution, as shown in Fig. 5 and Eq. (20).

Simulation environment of the DIPC system is shown in Fig. 6. By including the quantized encoder signals in the feedback loop, the model provides a realistic evaluation of system performance, making it possible to assess how the controller responds to measurement noise and quantization effects before conducting real-world experiments. The simulation models developed in this section serve as the foundation for subsequent experimental validation. By comparing the simulated responses with the actual system responses, the accuracy of the model and the effectiveness of the LQR controller can be thoroughly assessed.

$$\text{pulse} = \frac{\text{step} * 2}{\pi} \tag{19}$$

where:

step : Encoder resolution (pulses per round)

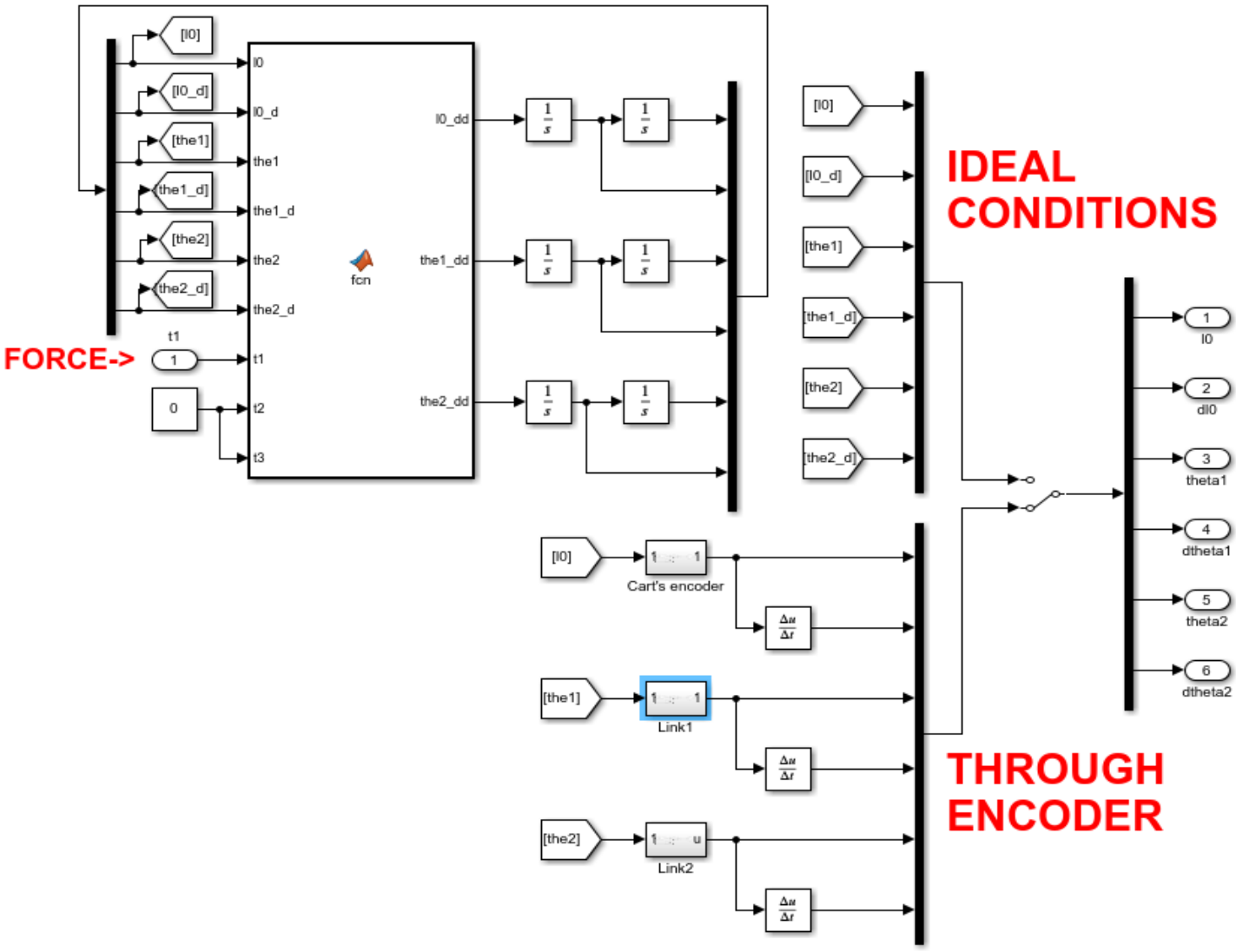

Fig. 3. Simulation of the DIPC system [29]

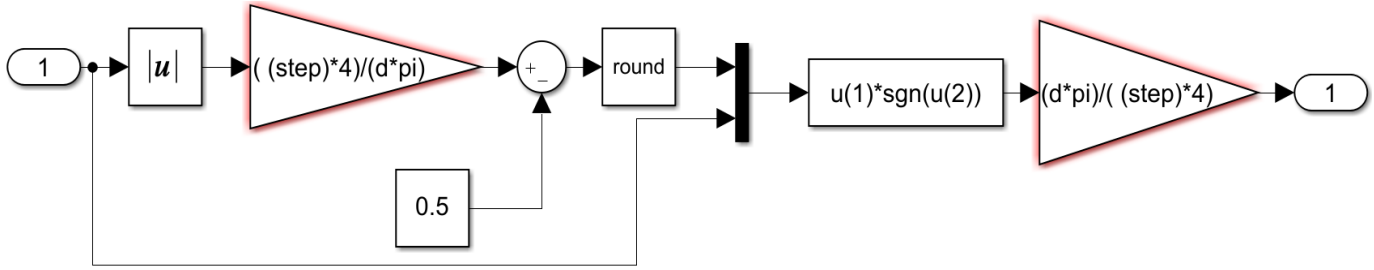

Fig. 4. Simulation of the cart's encoder [29]

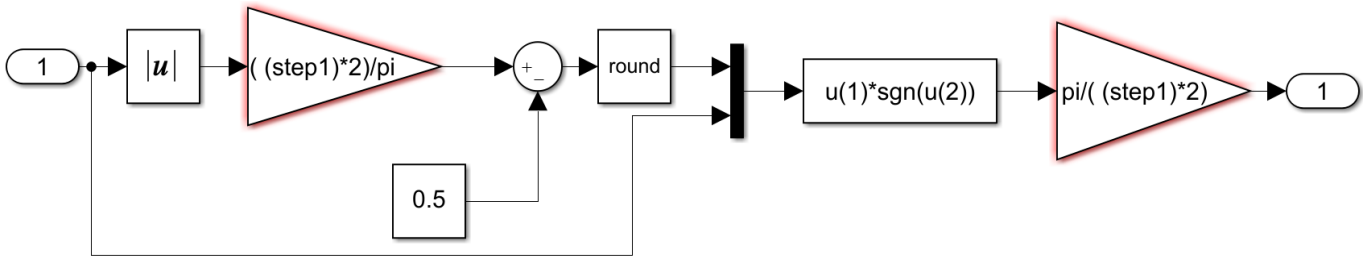

Fig. 5. Simulation of the encoder for pendulums [29]

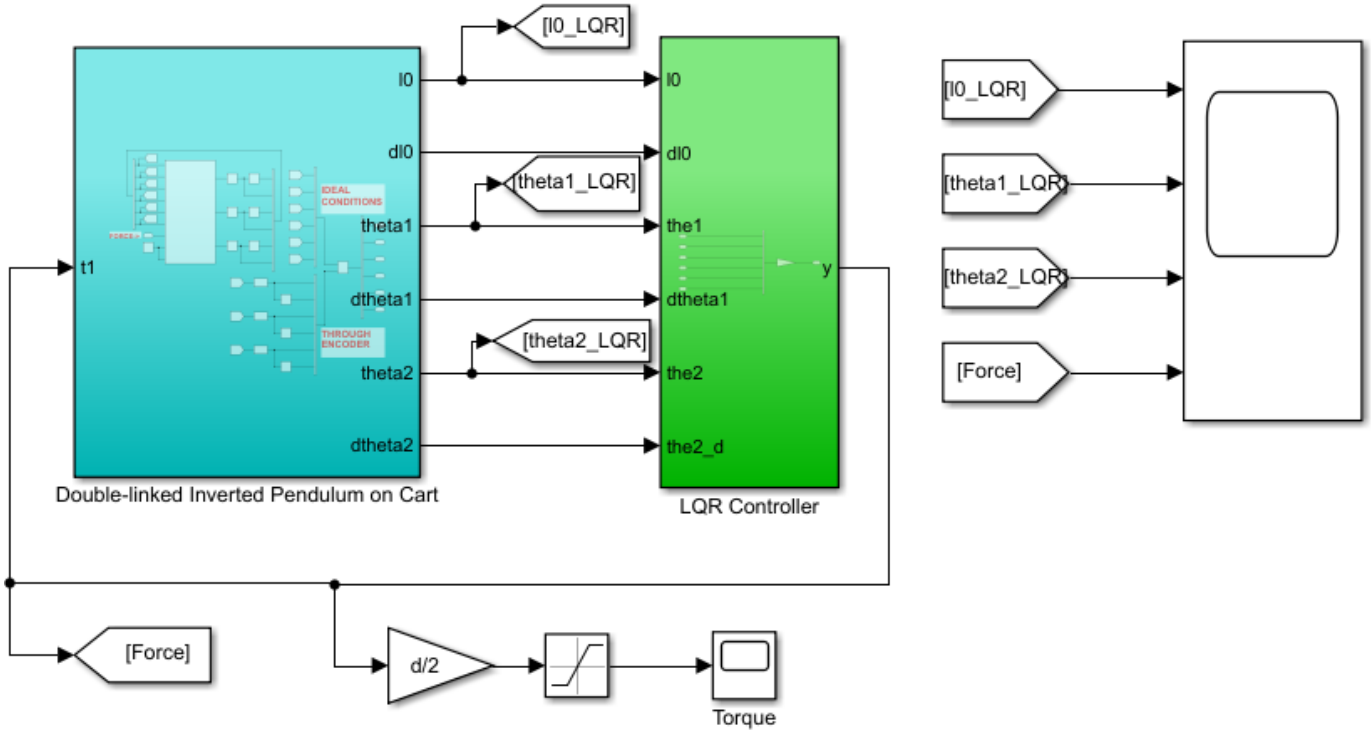

Fig. 6. Simulation of DIPC with an LQR controller [29]

3. Experimental setup

The hardware setup employed in this study is illustrated in Fig. 7 and Fig. 8 as follows:

1. Motor's encoder.
2. Link 1 and its encoder.
3. Link 2 and its encoder
4. NISCA DC motor.
5. Pulley transmission mechanism.
6. STM32F407G-DISC1.
7. BTS7960 H-Bridge circuit.
8. Encoder signal reading and UART circuit.
9. Power circuit breaker.

Fig. 9 illustrates the hardware connection diagram of the practical DIPC system.

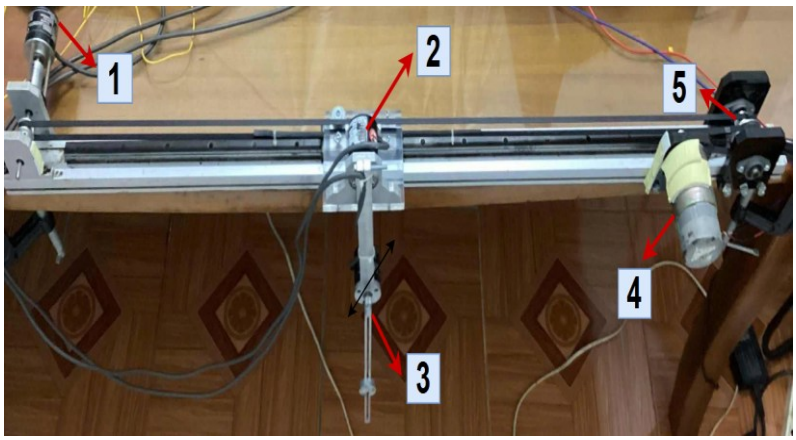

Fig. 7. Hardware setup of the DIPC system

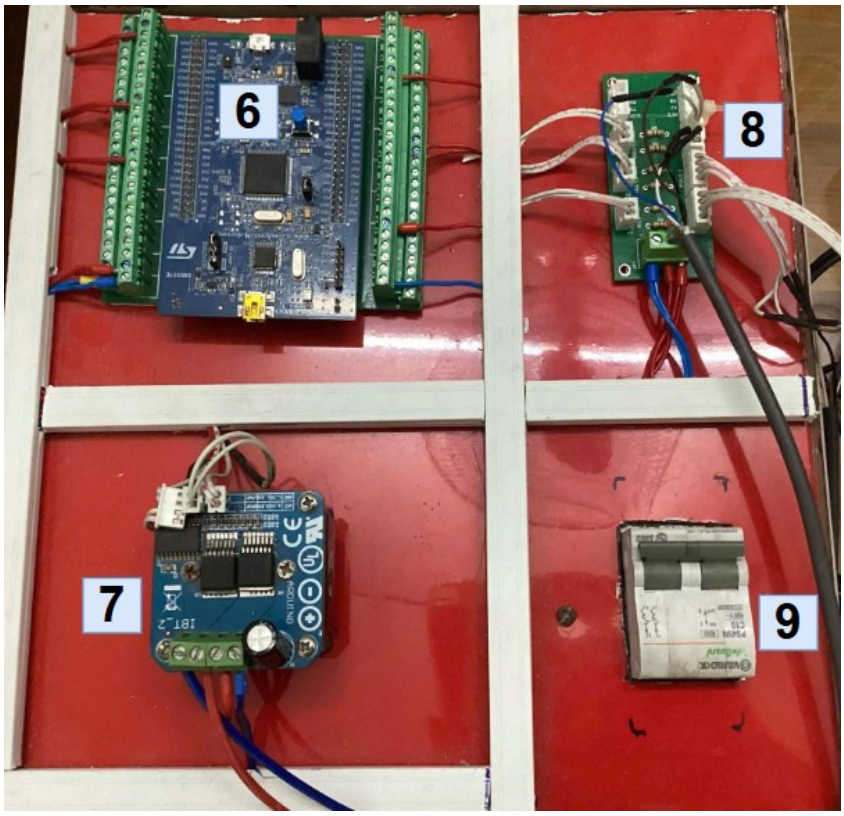

Fig. 8. Control circuit for the DIPC system

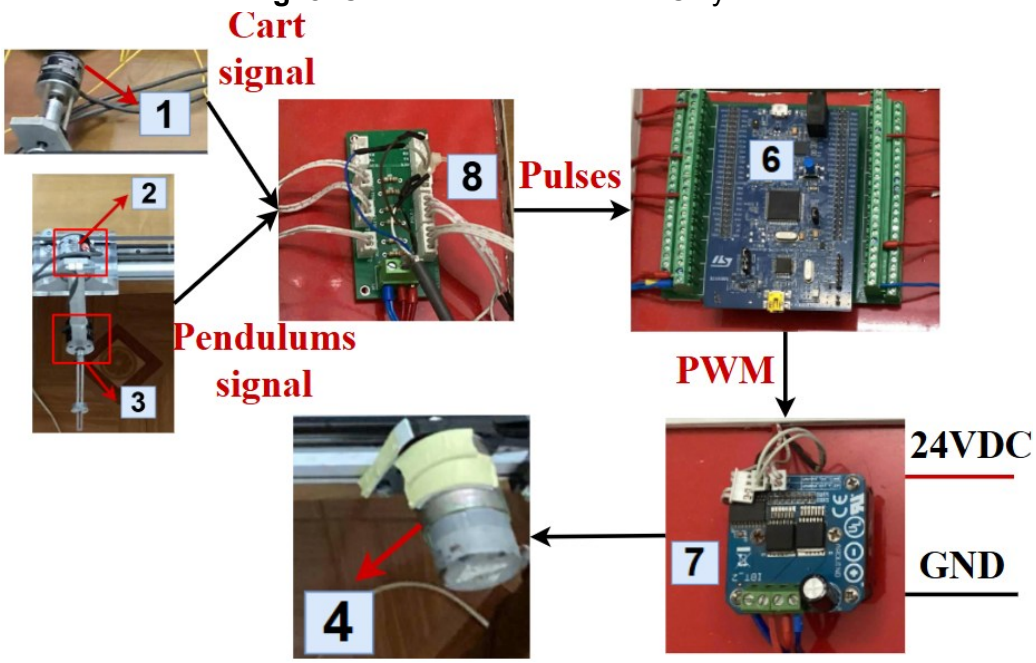

Fig. 9. Connection diagram

In the practical system, we employed the formula referenced from [22] to convert the torque into the required voltage supplied to the motor as follows:

$$e = \frac{R_m}{K_t}\tau + K_b\upsilon \quad (20)$$

where:

e: Voltage supplied to the motor (V)

τ: Motor torque (N.m)

υ: Angular speed of the motor (rad/s)

R_m: Motor resistance (Ohm)

K_b: Counter electric constant (V/(rad/sec))

K_t: Torque constant (N.m/A)

Fig. 10 illustrates the processing flow of the

DIPC system control program. The control workflow of the experimental DIPC system can be summarized as follows. The STM32F407G microcontroller reads the encoder pulses to compute the cart position and the angular deviations of both pendulums. If the cart remains within ±0.25 m, the first pendulum within ±45°, and the second pendulum within ±20°, the LQR controller is engaged to stabilize the system. The LQR output is then converted into torque and further transformed into a PWM voltage signal to drive the DC motor through an H-bridge. This closed-loop process is executed in real time to ensure stable operation of the pendulum system.

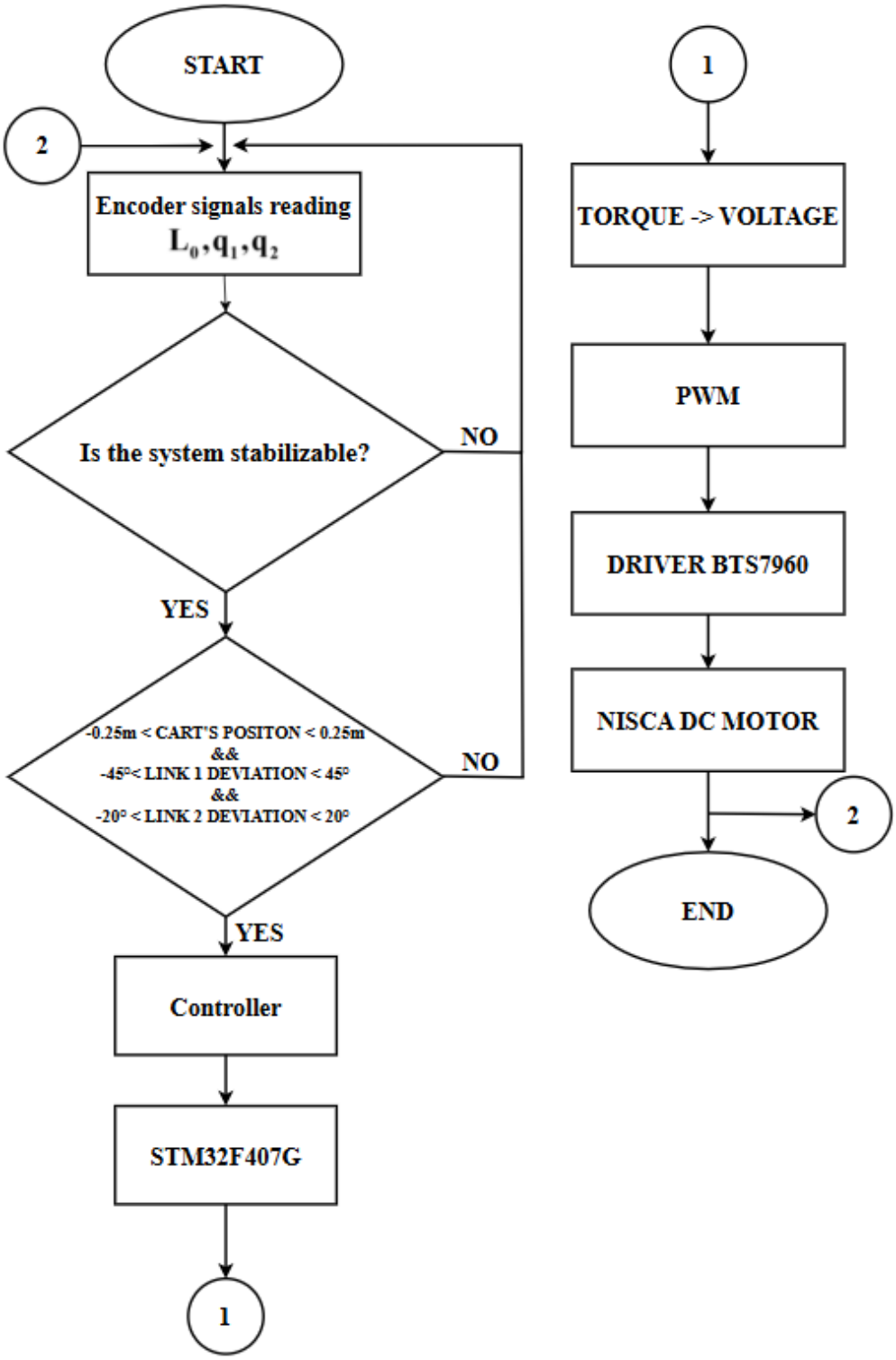

Fig. 10. Algorithm flowchart for DIPC system [28]

4. Results and Discussion

As mentioned earlier, the simulation study considers both ideal and non-ideal conditions. In the non-ideal case, the input signal resolution is reduced using an encoder simulation block to better represent practical implementation conditions. In addition, the simulation results are compared between the LQR controller presented in [29] and the newly proposed LQR controller in this study. This comparison allows the effectiveness and robustness of the new LQR controller to be evaluated more comprehensively. Furthermore, the analysis also helps assess the discrepancy between simulation and experimental results, thereby providing a clearer foundation for subsequent experimental implementation and system improvement. Both simulation and experimental studies were carried out in Simulink using MATLAB 2020a and the Waijung Blockset with a sampling time of 0.005s.

4.1. Simulation results

The initial value of the deviation angle of link 1 is set to 0.1 rad (~5.7°), while the deviation angle of link 2 is initialized at 0.15 rad (~8.6°).

In the ideal condition Fig. 11(a), a relatively large control force is initially applied to the cart in order to prevent the pendulums from falling, resulting in significant transient oscillations. The maximum cart displacement reaches approximately 0.88 m from the reference position, whereas the previous controller produced a larger displacement of 0.97 m. The system begins to reach a steady state at approximately 26.96 seconds, where the cart position converges to about 0.0019 m, corresponding to roughly 2% of the initial deviation of 0.14 m. In contrast, the previous controller required 71.14 seconds to reach the steady-state condition. These results indicate that the proposed controller prioritizes stabilizing the pendulums before regulating the cart position. Consequently, although the settling time of the cart is not extremely fast, it remains acceptable and feasible for practical implementation, while still providing a significant improvement compared with the previous controller.

Under the non-ideal condition Fig. 11(b), the simulation more closely reflects real-world operation due to the reduced input resolution. In this case, the maximum cart displacement is approximately 0.91 m, which is smaller than the 1.13 m observed with the previous controller. After the transient phase, the cart oscillates around the equilibrium position within a range of (−0.17, 0.16) m, whereas the previous controller exhibited a larger oscillation range of (−0.25, 0.41) m. If such behavior occurs in practice, it indicates that the system can still maintain an acceptable level of stability.

Under ideal conditions Fig. 12(a), the first pendulum is initially displaced by 0.1 rad from its upright equilibrium position. When the controller is activated, a relatively strong corrective control input is applied to stabilize both pendulums simultaneously. Due to the coupled dynamics of the double-link system, the first pendulum exhibits transient oscillations with a maximum deviation of approximately 0.478 rad, which is slightly larger than the 0.44 rad observed with the previous controller. Nevertheless, the system begins to reach a steady state at around 5.445 s, when the deviation of the first pendulum decreases to approximately 0.002 rad, corresponding to about 2% of the initial deviation. In comparison, the previous controller achieved a faster settling time of 2.24 s, gradually converging to the equilibrium position with a negligible steady-state error. Although the settling time of the first pendulum in this case is relatively slower, this behavior reflects the control strategy of the DIPC system, where the controller is designed to prioritize stabilizing the second pendulum, which exhibits stronger instability and has a more significant influence on the overall system dynamics. Consequently, accepting a slightly slower convergence of the first pendulum is reasonable, while the steady-state

error remains very small and the overall stability of the system is maintained.

Under non-ideal conditions Fig. 12(b), where the input resolution is reduced to emulate practical measurement limitations, the maximum deviation of the first pendulum is approximately 0.465 rad. After about 2 s, the pendulum oscillates around the equilibrium position with an amplitude within (−0.05, 0.04) rad. This oscillation range is smaller than that of the previous controller, which fluctuates within (−0.07, 0.07) rad and occasionally expands to (−0.08, 0.08) rad. These results indicate that the proposed controller effectively reduces the oscillation amplitude around the equilibrium point, thereby improving the stability and precision of the system under conditions that are closer to real-world operation. In practical implementations, such oscillation levels are considered acceptable and demonstrate that the system maintains reliable stabilization performance.

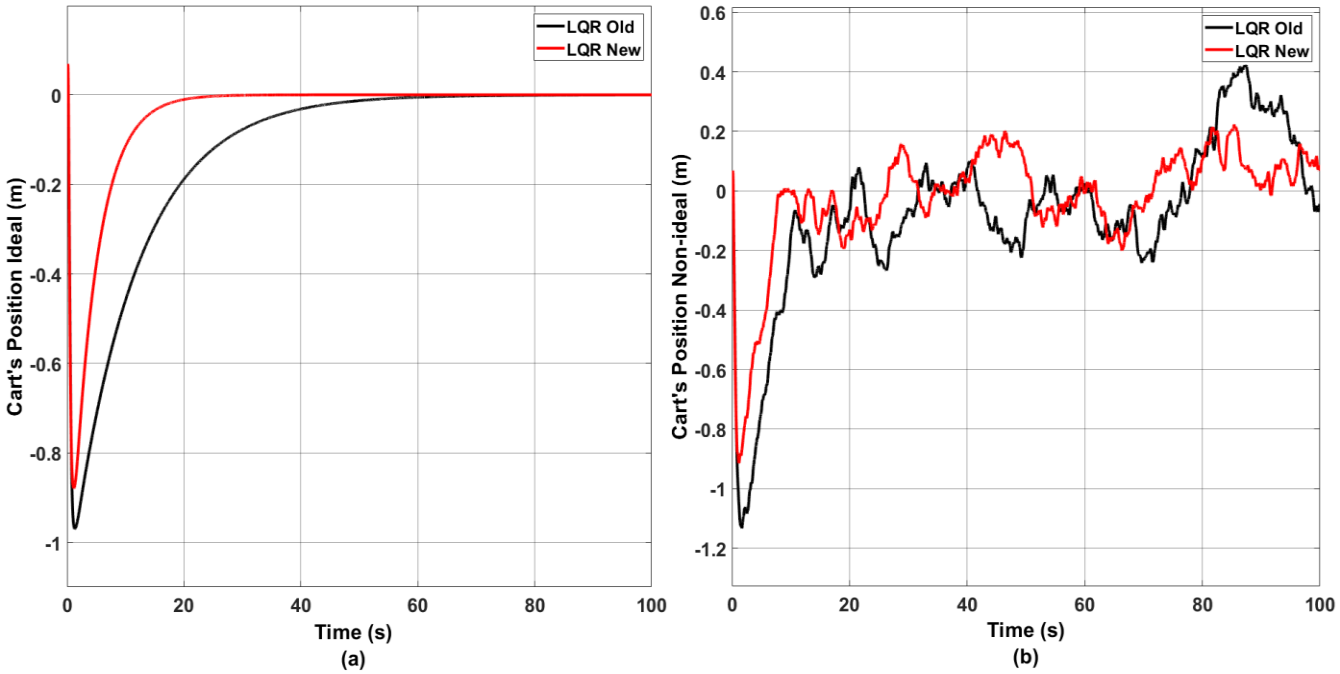

Fig. 11. The cart position response (a) under ideal conditions, (b) under non-ideal conditions

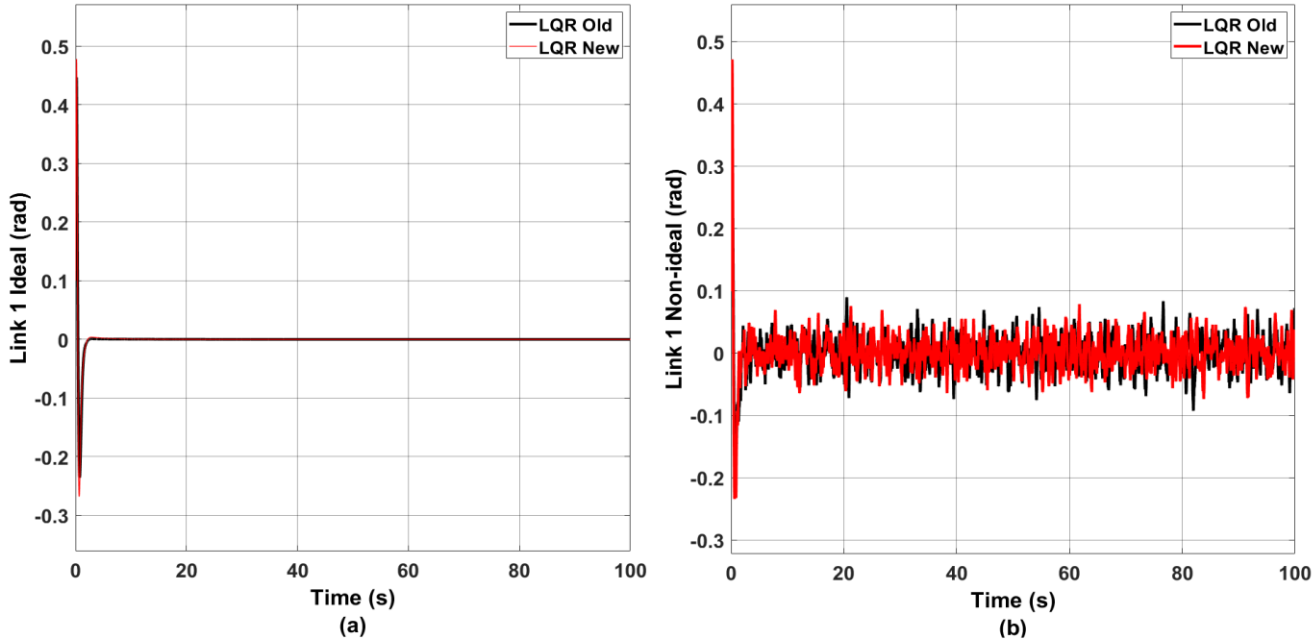

Fig. 12. The first pendulum's response (a) under ideal conditions, (b) under non-ideal condition

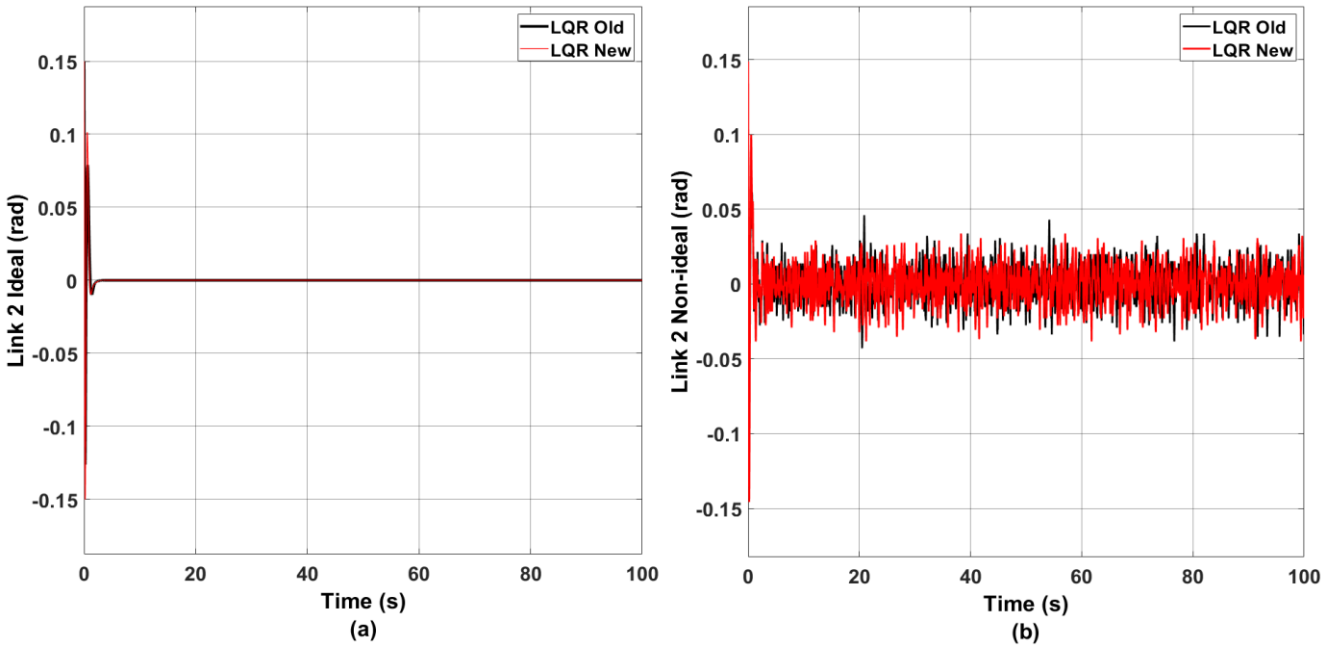

Fig. 13. The second pendulum's response (a) under ideal conditions, (b) under non-ideal condition

Under ideal conditions Fig. 13(a), the second pendulum is initially displaced by 0.15 rad from its upright equilibrium position. When the controller is activated, a strong corrective control input is applied to stabilize the system, with higher priority assigned to the second pendulum due to its higher level of instability in the DIPC structure. During the transient phase, the second pendulum oscillates and reaches a maximum deviation of approximately −0.15 rad, which is slightly larger than the −0.125 rad observed with the previous controller. Nevertheless, the system rapidly reaches a steady state at around 1.91 s, when the deviation of the second pendulum decreases to approximately 0.002 rad, corresponding to about 2% of the initial deviation, and then gradually converges to the equilibrium position with a negligible steady-state error. Compared with the previous controller, which required 1.96 s to settle, the proposed controller demonstrates a slight improvement in settling time while maintaining high steady-state accuracy.

Under non-ideal conditions Fig. 13(b), where the input resolution is reduced to better emulate practical measurement conditions, the maximum deviation of the second pendulum is approximately −0.14 rad. After about 1.7 s, the pendulum oscillates around the equilibrium position with an amplitude within (−0.02, 0.02) rad, occasionally expanding slightly to (−0.04, 0.04) rad. From the graph, it can be observed that the oscillation amplitude produced by the proposed controller is smaller than that of the previous controller, indicating improved stability when the system operates under non-ideal conditions. In practical applications, such oscillation levels are considered acceptable and demonstrate that the system is capable of maintaining reliable stabilization performance.

Under ideal conditions Fig. 14(a), when both pendulums initially deviate significantly from the equilibrium position, the controller generates a relatively large control force to rapidly restore the system to a stable state. Specifically, the force applied to the cart reaches a maximum value of approximately 23 N during the initial transient phase. As the pendulums gradually approach the upright equilibrium, the control force decreases progressively and converges toward 0 N, indicating that the controller effectively regulates the control effort as the system stabilizes.

Under non-ideal conditions Fig. 14(b), where the input resolution is reduced to better emulate practical operating conditions, the control force primarily oscillates within the range (–10, 10) N,

occasionally increasing to approximately (–13.3, 13.6) N. Overall, in both scenarios, the applied force remains within a reasonable range considering the mechanical parameters and actuator capabilities of the system. Notably, when compared with the previous controller, the proposed controller exhibits smaller control force amplitudes, indicating that it utilizes control energy more efficiently while still maintaining effective stabilization performance.

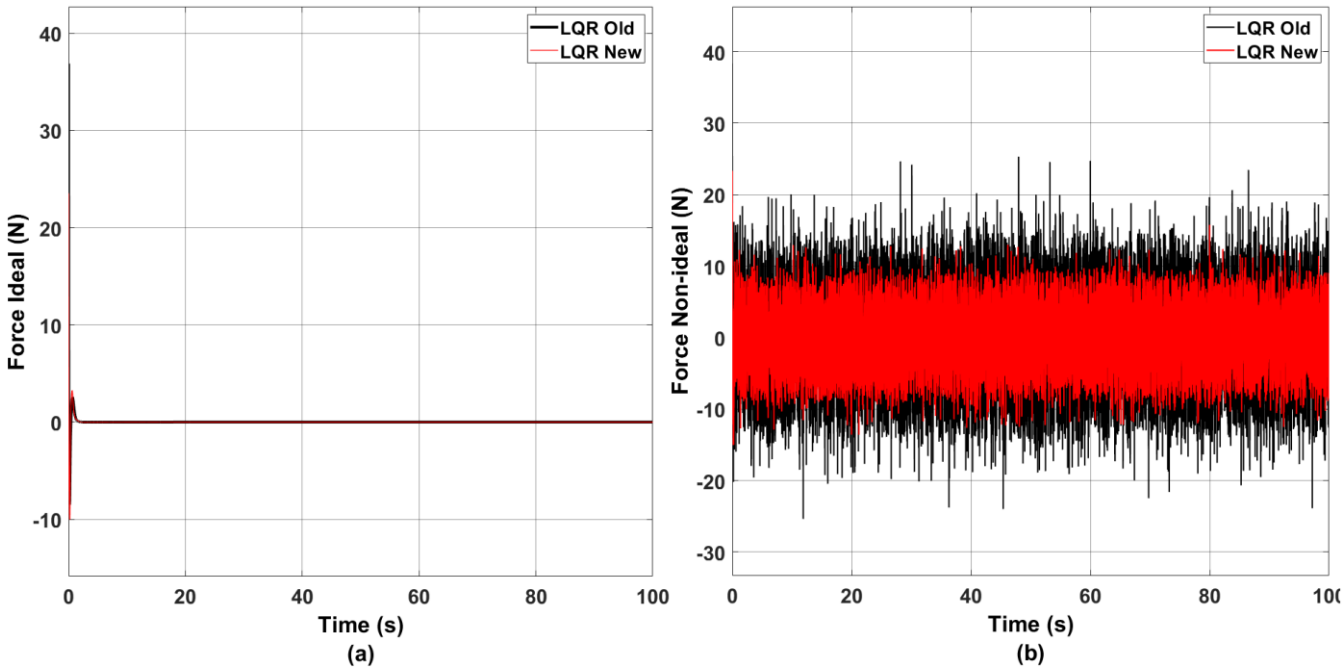

Fig. 14. Applied force on the cart (a) under ideal conditions, (b) under non-ideal conditions

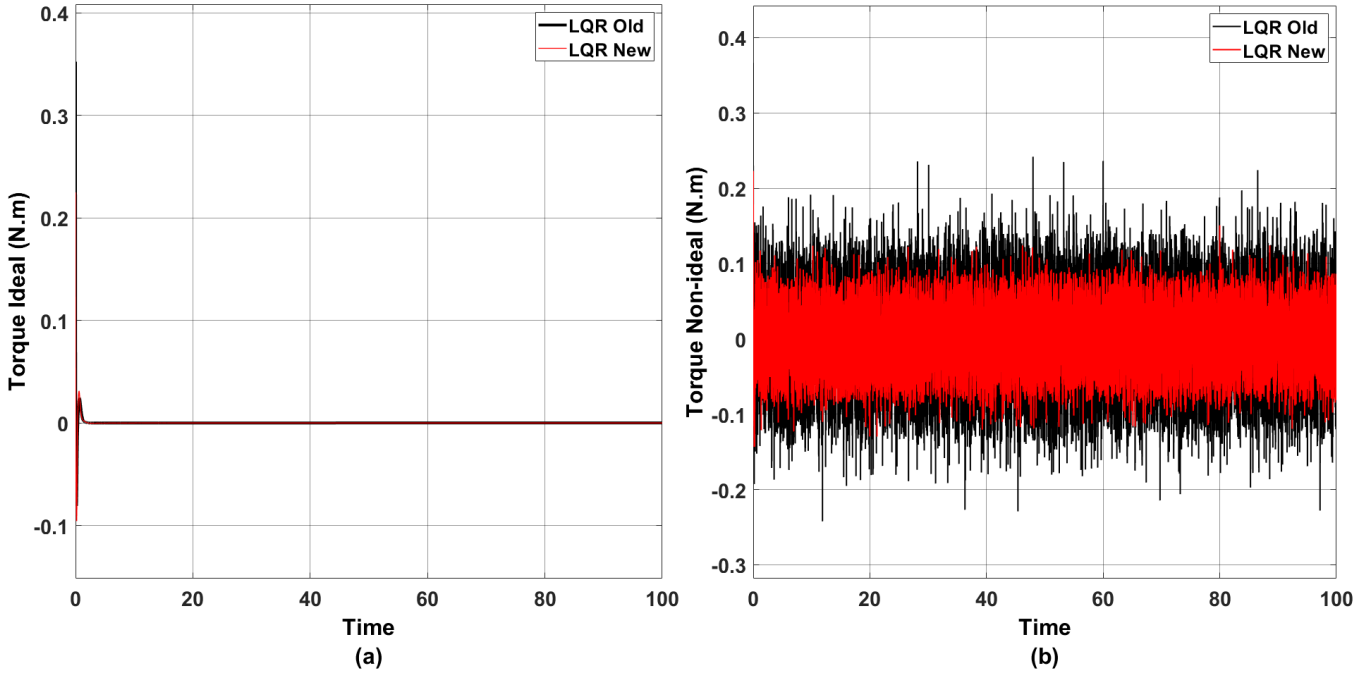

Fig. 15. Applied torque on the cart (a) under ideal conditions, (b) under non-ideal conditions

To further evaluate the influence of the control force on the drive mechanism, the force was converted into torque by multiplying it with the pitch radius of the pulley, thereby estimating the torque applied to the system. The results shown in Fig. 15(a) and Fig. 15(b) indicate that the initial torque reaches a relatively high magnitude of approximately 0.22 N.m, enabling the system to quickly recover toward the equilibrium state. As the system stabilizes, the torque gradually decreases

toward 0 N.m under ideal conditions. Under non-ideal conditions, the torque oscillates within approximately (−0.13, 0.13) N.m, reflecting the continuous adjustments made by the controller to maintain system balance. These torque values remain within the safe operating range of the actuation mechanism and provide an important reference for evaluating and tuning the hardware configuration to satisfy the system's operational requirements.

To quantitatively evaluate the control performance, the Root Mean Square Error (RMSE) was employed as a performance metric. The RMSE provides a statistical measure of the deviation between the desired state and the actual system response over the observation period. It is defined as:

$$\mathrm{RMSE} = \sqrt{\frac{1}{T}\sum_{i=1}^{T}\left(s_i - s_{ref}\right)^2} \quad (21)$$

where s_i denotes the measured state variable at sample I, s_{ref} is the desired equilibrium value, and T represents the total number of samples.

Table 2. Quality of DIPC according to the RMSE Standard (Under Non-ideal Simulation)

Response of system	LQR Controller	
	Old	New
Cart (m)	0.2809	0.1608
Link1 (rad)	0.0348	0.0362
Link2 (rad)	0.0133	0.0145
Torque (Nm)	0.0599	0.0378

Table 2 presents the RMSE values of the system responses under non-ideal simulation conditions. It can be observed that the proposed LQR controller significantly improves the cart position accuracy, reducing the RMSE from 0.2809 m to 0.1608 m. In addition, the control effort is reduced, as reflected by the decrease in torque RMSE from 0.0599 Nm to 0.0378 Nm, indicating a more energy-efficient control action. Although the RMSE values of Link1 and Link2 are slightly higher compared with the previous controller, the differences remain relatively small and do not significantly affect the overall stabilization performance. Overall, the results suggest that the proposed LQR controller achieves better cart regulation while maintaining comparable pendulum stability with lower control effort.

4.2. Experimental results

When applying the feedback gain matrix K obtained from the simulation to the real system, we observed that the control action associated with the angular velocity of the second pendulum was relatively large, leading to strong oscillations and preventing the system from maintaining balance. This phenomenon is mainly attributed to practical factors that are not fully captured in the simulation model, such as friction, actuator limitations, and measurement noise. Consequently, the last element of the matrix K, which corresponds to the angular velocity of the second pendulum, was reduced from 24.7514 to 14.7514, while keeping the other elements unchanged. This adjustment helps reduce excessive control effort and improves the damping behavior of the system, thereby enhancing the stability and robustness of the real-time implementation.

In the experimental setup, the initial deviation of pendulum 1 was set to approximately 0 rad, and that of pendulum 2 to about 0.348 rad (~20°). The actual system response over 40 seconds is illustrated in the graph below.

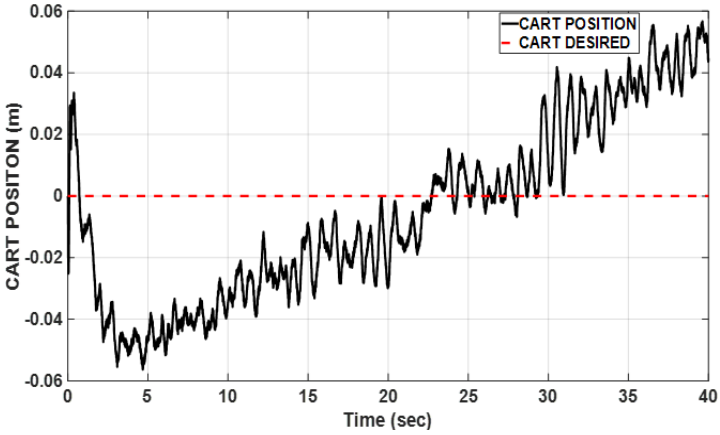

Fig. 16. Experimental response of cart position

Fig. 16 illustrates the cart position response. Initially, due to the relatively large deviation of the

second pendulum (~20°), the force acting on the cart was also large in order to rapidly counteract the fall of both pendulums. As a result, the cart exhibited significant oscillations, reaching up to 0.06m from its initial position (0 m). Once the pendulums gradually stabilized, the cart continued to move toward 0m while still prioritizing the upright balance of the pendulums. Consequently, the cart approached the equilibrium position in approximately 20s. At this stage, its position oscillated within the range of (-0.02, 0.02) m and maintained this behavior for the next 10s. After more than 30s of operation, accumulated errors in measuring the pendulum deviation led to stronger oscillations to maintain balance. Nevertheless, the oscillation amplitude remained small (<0.01 m), which can still be considered a safe and acceptable operating region. The experimental results indicate that the oscillation amplitude is significantly smaller than that obtained in the simulation.

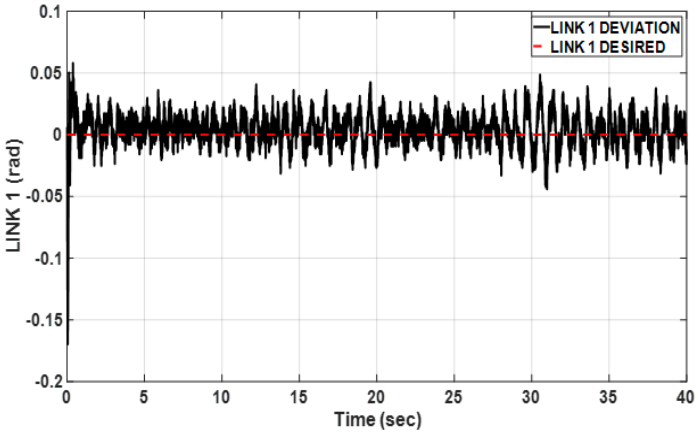

Fig. 17. Experimental response of the first pendulum angle

Fig. 17 presents the actual deviation response of the first pendulum. When the controller acted on the cart, the first pendulum exhibited a maximum oscillation amplitude of approximately 0.17 rad (~10°). However, this oscillation was relatively small and rapidly diminished; within about 0.38 s, the amplitude narrowed to the range of (−0.05, 0.05) rad, remaining mostly stable within (−0.03, 0.03) rad. The experimental results indicate that the first pendulum maintained a nearly stationary state.

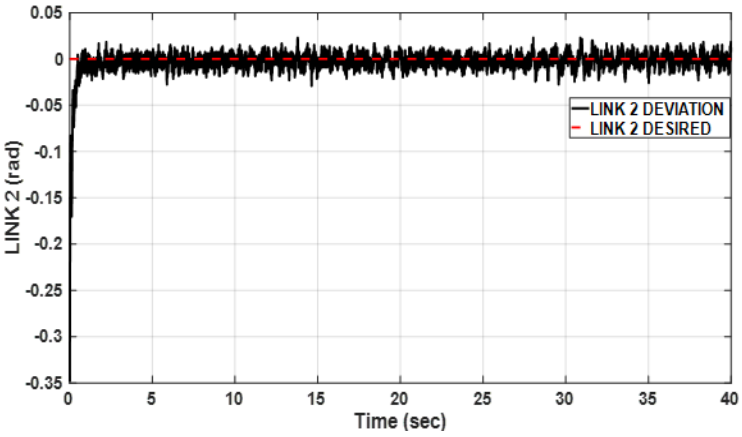

Fig. 18. Experimental response of the second pendulum angle

Fig. 18 shows the actual deviation response of the second pendulum. Initially, the pendulum was displaced by about –0.348 rad from the equilibrium position. When the controller acted on the cart, the deviation was quickly driven back toward equilibrium, reaching a peak oscillation of approximately 0.06 rad. The entire process took only about 0.57 s for the deviation to enter the range of (−0.03, 0.03) rad and remain continuously stable within this region. While the first pendulum still exhibited slight oscillations, the second pendulum was nearly stationary, showing virtually no oscillatory behavior. The experimental response of two pendulums shows a strong similarity to the simulation results.

Fig. 19 illustrates the torque acting on the cart. The data from the six state variables were multiplied by the LQR gain matrix K to obtain the control force. This force was then converted into the required torque based on the lever arm principle. Subsequently, the formula presented in Eq. (21) was applied to convert torque into voltage. The resulting motor supply voltage, shown in Fig. 20, corresponds to the voltage required to generate the desired torque.

The experimental results revealed a considerable discrepancy in torque between simulation and practice. The reason is that, if only the conventional approach is applied-converting force into torque and then computing the motor supply voltage-the motor and transmission system

cannot generate sufficient torque to move the cart. Therefore, we introduced an additional compensation factor of gain = 3 to account for system losses. As a result, the motor supply voltage remained relatively high, mostly within 40–70% of the maximum voltage (24 VDC), even when the system was in a balanced state. Consequently, after maintaining equilibrium for more than 4 minutes, the motor gradually heated up. Nevertheless, the overall system response can still be considered satisfactory.

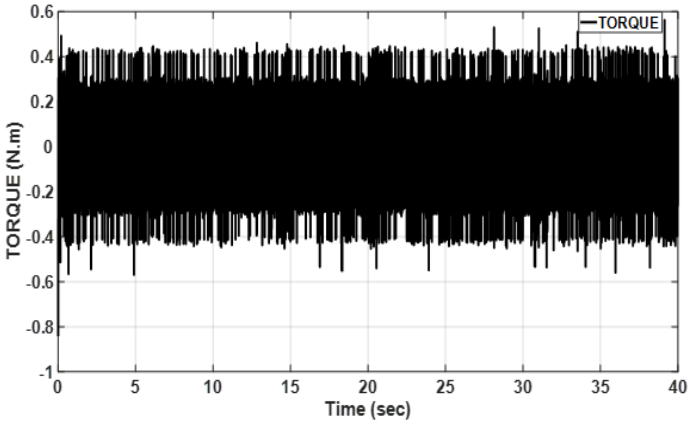

Fig. 19. Actual torque acting on the cart

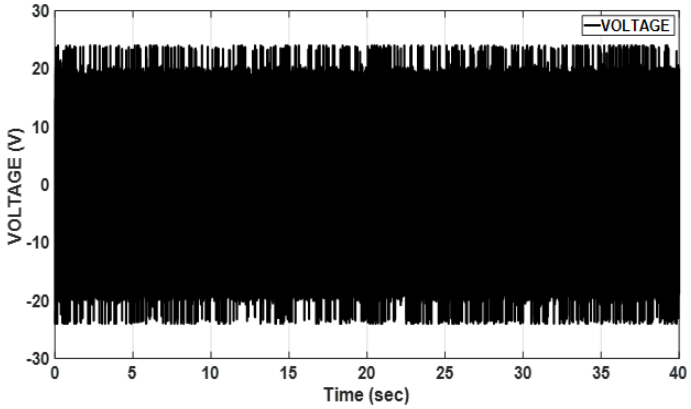

Fig. 20. Actual voltage supplied to the motor

Table 3. Quality of DIPC according to the RMSE Standard

Response of system	LQR Controller	
	Simulation (New)	Experiment
Cart (m)	0.1608	0.0299
Link1 (rad)	0.0362	0.0144
Link2 (rad)	0.0145	0.0135
Torque (Nm)	0.0378	0.2225

Table 3 summarizes the RMSE values obtained from both simulation and experimental results for the cart position, the angular deviations of the two pendulum links, and the control torque. These results provide a quantitative comparison between the simulated model and the real-world implementation of the controller.

It can be observed that the RMSE values of the pendulum angles in the experiment are comparable to, and in some cases smaller than, those obtained in simulation. In particular, the RMSE of Link 1 decreases from 0.0362 rad in simulation to 0.0144 rad in the experiment, while the RMSE of Link 2 shows a slight improvement from 0.0145 rad to 0.0135 rad. These results indicate that the experimental controller is capable of maintaining the upright equilibrium of the DIPC system with high accuracy.

For the cart position, the experimental RMSE (0.0299 m) is significantly smaller than that obtained in simulation (0.1608 m). This indicates that the cart motion in the real system is more constrained during the balancing process. Such behavior is mainly attributed to physical factors present in the experimental setup, including mechanical friction in the rail mechanism, actuator limitations, and other unmodeled damping effects. These factors naturally reduce excessive cart oscillations, resulting in improved position stability compared to the idealized simulation model.

On the other hand, the RMSE of the control torque in the experiment (0.2225 Nm) is higher than that in simulation (0.0378 Nm), indicating that the real system requires a larger control effort to maintain stability. This phenomenon is mainly caused by unmodeled disturbances, measurement noise, and nonlinear effects present in the physical system.

Overall, the RMSE analysis confirms that the proposed controller can effectively stabilize the DIPC system in practice while maintaining acceptable tracking accuracy.

5. Conclusion

In this study, we successfully implemented

experimental control of a highly nonlinear system, DIPC system. The experimental responses were generally satisfactory and closely matched the simulation results in terms of the deviation angles of both pendulums. For the cart position, the experimental performance was even better than in simulation. However, achieving such high-quality responses required relatively high energy consumption, even when the system was already in a balanced state.

These results provide a foundation for further optimization of the system's performance in terms of both state variable responses and energy efficiency in future research. Moreover, the scope of experimentation will be expanded to include other control approaches such as intelligent control, nonlinear control, and trajectory tracking control.

Acknowledgments

This research was funded by Ho Chi Minh City University of Technology and Engineering, Vietnam, under grant No. T2026-177. We, authors, are grateful to those supports. Link of operation of system is: https://youtu.be/TJdGgjHxqBg.

References

[1] O. Boubaker. (2013). The inverted pendulum benchmark in nonlinear control theory: A survey. *International Journal of Advanced Robotic Systems*, 10(5), 233:2013. https://doi.org/10.5772/55058

[2] K.H. Lundberg, T.W. Barton. (2010). History of inverted-pendulum systems. *IFAC Proceedings Volumes*, 42(24), 131–135. doi: 10.3182/20091021-3-JP-2009.00025

[3] D.A. Duy, L.H. Phuong, V.D. Cong. (2021). Stability analysis and assessment of double inverted pendulum with LQR and LQG controllers. *Journal of Mechanical Engineering Research and Developments*, 44(10), 408–417.

[4] N.Bandari, A. Hooshiar, Masoudrazban, Javaddargahi, C.-Y. Su. (2017). Stabilization of double inverted pendulum on cart: LQR approach. *International Journal of Mechanical and Production Engineering*, 5(2), 144-148.

[5] K. Ogata. (2010). Modern Control Engineering, 5th ed. *Prentice Hall*.

[6] C.-H. Nguyen, V.-S. Tran, X.-H. Nguyen, Q.-B. Truong, M.-T. Nguyen, N.-P. Luong, K.-V. Ngo, D.-H. Nguyen, T.-T. Nguyen, T.-T.-H. Le. (2024). ANFIS-based LQR control for rotary double parallel inverted pendulum. *Journal of Fuzzy Systems and Control*, 2(2), 109–116. doi: 10.59247/jfsc.v2i2.214

[7] S. Sanjeewa, M. Parnichkun. (2022). Control of rotary double inverted pendulum system using LQR sliding surface based sliding mode controller. *Journal of Control and Decision*, 9(1), 89–101. doi: 10.1080/23307706.2021.1914758

[8] Z.B. Hazem, M.J. Fotuhi, Z. Bingül. (2020). Development of a fuzzy-LQR and fuzzy-LQG stability control for a double link rotary inverted pendulum. *Journal of the Franklin Institute*, 357(15), 10529–10556. doi: 10.1016/j.jfranklin.2020.08.030

[9] K. Andrzejewski, M. Czyżniewski, M. Zielonka, R. Łangowski, T. Zubowicz. (2019). A comprehensive approach to double inverted pendulum modelling. *Archives of Control Sciences*, 29(3), 459–483. doi: 10.24425/acs.2019.130201

[10] S. Khatoon, D.K. Chaturvedi, N. Hasan, M. Istiyaque. (2017). Optimal control of a double inverted pendulum by linearization technique. *2017 International Conference on Multimedia, Signal Processing and Communication Technologies (IMPACT)*, pp. 123–127. doi: 10.1109/MSPCT.2017.8363988

[11] V. Mohan, A. Rani, V. Singh. (2017). Robust adaptive fuzzy controller applied to double inverted pendulum. *Journal of Intelligent & Fuzzy Systems: Applications in Engineering and Technology*, 32(5), 3669–3687. doi: 10.3233/JIFS-169301

[12] L. Moysis. (2016). Balancing a double inverted

pendulum using optimal control and Laguerre functions. doi: 10.13140/RG.2.1.2948.6486

[13] E. Shala, X. Bajrami, R. Likaj, A. Pajaziti. (2023). Real-time swinging up and stabilizing a double inverted pendulum using PID-LQR. *Journal of Mechanical Engineering*, 73(1), 159–168. doi: 10.2478/scjme-2023-0013

[14] S.K. Yadav, S. Sharma, N. Singh. (2012). Optimal control of double inverted pendulum using LQR controller. *International Journal of Advanced Research in Computer Science and Software Engineering*, 2(2), 189–192.

[15] Y. Yaren, S. Kizir. (2021). Power-based modelling and control: experimental results on a cart-pole doubleinverted pendulum. *Turkish Journal of Electrical Engineering and Computer Sciences,* 29(3), 1736-1750. doi: 10.3906/elk-2006-68

[16] P. Shen. (2015). ANFIS control double-inverted pendulum. *Chemical Engineering Transactions*, 46, 895–900. doi: 10.3303/CET1546150

[17] J.-S.R. Jang. (1993). ANFIS: Adaptive-network-based fuzzy inference system. *IEEE Transactions on Systems, Man, and Cybernetics*, 23, 665–685. doi: 10.1109/21.256541

[18] M.D. Tran, M.T. Vo, Q.M. Pham, D.T. Nguyen, H.T. Vo, N.T. Tran, D.D. Le, L.V. Nguyen, A.K. Tran, C.H. Phan. (2023). Swing-up and stabilization control of rotary inverted pendulum by using LQR-based ANFIS (in Vietnamese). *Journal of Science and Technology – Binh Duong University*, 6(1), 137-146. doi: 10.56097/binhduonguniversityjournalofscience andtechnology.v6i1.96

[19] H. Niemann, J. Stoustrup. (2005). Passive fault tolerant control of a double inverted pendulum: A case study. *Control Engineering Practice*, 13(8), 1047–1059. doi: 10.1016/j.conengprac.2004.11.002

[20] M.R. Nalavade, M.J. Bhagat, V.V. Patil. (2014). Balancing double inverted pendulum on a cart by linearization technique. *International Journal of Recent Technology and Engineering*, 3(1), 153-157.

[21] S. Qiang, Q. Zhou, X.Z. Gao, S. Yu. (2008). ANFIS controller for double inverted pendulum. Proc. *6th IEEE International Conference on Industrial Informatics, pp. 475–480*. doi: 10.1109/INDIN.2008.4618147

[22] T.-B. Tran, T.-K.-V. Dang, M.-N. Phan, B.-D. Tran, V.-D. Trinh, H.-Q.-B. Nguyen, T.-T.-T. Vo, T.-T.-H. Le. (2024). A survey of identification experimental system parameters using genetic algorithm. *Robotica & Management*, 29(1), 39–44. https://doi.org/10.24193/rm.2024.1.7

[23] D.-P. Hoang, H.-A. Nguyen, Q.-S. Pham, H.-C. Pham, M.-S. Huynh, D.-P. Phan, N.-T. Truong, D.-P. Nguyen, T.-T.-U. Nguyen, H.-T. Nguyen. (2024). A survey of experimental LQR for cart and pole. *Journal of Fuzzy Systems and Control*, 2(2), 97–103. doi: https://doi.org/10.59247/jfsc.v2i2.211

[24] I. Chawla, V. Chopra, A. Singla. (2019). Robust LQR based ANFIS control of x-z inverted pendulum. *Proceedings of 2019 Amity International Conference on Artificial Intelligence (AICAI), pp. 818–823*. doi: 10.1109 / AICAI.2019.8701333

[25] H.A. Elmasrub, A.D. Elgodban, M.H. Zayed. (2016). The inverted pendulum in nonlinear control theory: A review. *Proceedings of 3rd International Conference on Automation, Control, Engineering and Computer Science, pp. 921-925.*

[26] S. Irfan, L. Zhao, S. Ullah, A. Mehmood, M.F.U. Butt. (2024). Control strategies for inverted pendulum: A comparative analysis of linear, nonlinear, and artificial intelligence approaches. *PLoS ONE*, 19(3), e0298093. doi: 10.1371/journal.pone.0298093

[27] T.V. Do, T.N. Ho, M.T. Nguyen, V.D.H. Nguyen. (2017). Balancing control for double-linked inverted pendulum on cart: Simulation and experiment. *Journal of Technical Education*

Science, 12(2), 68–75.

[28] T.-P.-N. Pham et al. LQR-based information fusion fuzzy control for experimental double inverted pendulum on cart. *Robotica & Management*, 31(1), 2026, accepted for publication.

[29] T.-P.-N. Pham, T.-B. Tran, V.-D.-H. Nguyen, T.-T. Nguyen, G.-T. Nguyen, D.-P. Nguyen, D.-K. Nguyen, V.-A. Ha, T.-N.-C. Trinh, T.-T. Nguyen. (2025). An LQR-based ANFIS control for double-linked inverted pendulum on cart. *Journal of Fuzzy Systems and Control*, 3(2), pp. 135–141. doi: 10.59247/jfsc.v3i2.307

[30] J.J. Craig. (2005). Introduction to Robotics: Mechanics and Control, 3rd ed. *USA: Pearson Education*.